RSC Advances

PAPER

View Article Online
View Journal | View Issue

Cite this: *RSC Adv.*, 2026, **16**, 28909

Decoding structural rigidity and charge-transfer polarization in barbituric-acid-based donor–π–acceptor chromophores

Keerthi Miryala, Mihika Katdare and Nilanjan Dey *

Two barbituric-acid-based donor–π–acceptor chromophores were systematically investigated using density functional theory (DFT), time-dependent DFT, and solvent-dependent polarizable continuum model (PCM) calculations to elucidate the interplay between molecular structure, excited-state electronic redistribution, reactivity, and photovoltaic relevance. Excited-state geometry optimizations revealed that compound 1 retained nearly invariant bond lengths and strict planarity upon $S_0 \rightarrow S_1$ excitation, indicating minimal structural relaxation with a predominantly locally excited (LE) character. In contrast, compound 2 showed pronounced excitation-induced bond-length modulation along the donor–acceptor axis, which was consistent with significant intramolecular charge transfer (ICT). Mulliken charge analysis, electrostatic potential mapping, and frontier molecular orbital distributions further confirmed the delocalized electronic excitation in 1 and strong donor-to-acceptor charge migration in 2. Solvent-dependent studies demonstrated a weak dielectric sensitivity for 1, whereas 2 exhibited enhanced polarization, solvent-tunable HOMO–LUMO gaps, and greater stabilization in polar media. Quantitative photovoltaic descriptors, including electron-injection driving force, excited-state dipole moment, light-harvesting efficiency, and reorganization energy, revealed that 2 possessed a favorable energetic alignment for electron injection into TiO_2, large excited-state polarization, and superior absorption efficiency, establishing its suitability as a dye sensitizer for dye-sensitized solar cell (DSSC) applications. In contrast, 1 exhibited marginal electron-injection capability and limited excited-state charge separation, restricting its photovoltaic applicability.

Received 26th January 2026
Accepted 7th April 2026

DOI: 10.1039/d6ra00689b

rsc.li/rsc-advances

Introduction

Barbituric acid-based charge-transfer (CT) dyes represent a versatile and structurally tunable class of push–pull chromophores, in which the electron-withdrawing barbituric acid core functions as an efficient acceptor when conjugated to π-bridges and electron-donating groups.[1] Owing to its imide-rich framework, high resonance stabilization, and multiple carbonyl functionalities, barbituric acid imparts pronounced electron affinity, strong intramolecular hydrogen-bonding capability, and enhanced stabilization of polarized excited states.[2] When incorporated into donor–π–acceptor architectures, these features promote strong intramolecular charge transfer, leading to broad and red-shifted absorption bands, large Stokes shifts, and high sensitivity of the optical response to the surrounding environment.[3] Consequently, barbituric acid–based CT dyes have found widespread application in nonlinear optics, organic photovoltaics, and optoelectronic devices, where a strong ICT character facilitates efficient charge separation and transport.[4] Their pronounced solvatochromism and polarity-dependent emission make them particularly attractive for chemical sensing, bioimaging, and environmental monitoring[5] Moreover, the robust hydrogen-bonding and aggregation-prone nature of the barbituric acid motif has been exploited in supramolecular assemblies, stimuli-responsive materials, and aggregation-induced emission systems.[6]

On the other hand, subtle structural variations in CT dyes, such as heteroatom substitution, modulation of donor or acceptor strength, alteration of π-bridge length, and changes in molecular planarity, can profoundly influence their photophysical and optical properties by directly governing excited-state electronic redistribution.[7] Structural rigidification or enhanced planarity generally increases π-conjugation and orbital overlap, leading to relatively high oscillator strengths, reduced nonradiative decay, and locally excited–dominated transitions with weak solvatochromism. In contrast, increased donor–acceptor asymmetry, bond-length alternation, or torsional flexibility promotes intramolecular charge transfer, resulting in red-shifted absorption/emission, large Stokes shifts, enhanced solvent sensitivity, and pronounced excited-state dipole moments.[8] Thus, understanding these structure–property relationships is critically important because photophysical performance ultimately determines the efficiency and

Department of Chemistry, Birla Institute of Technology and Science, Pilani Hyderabad, Telangana-500078, India. E-mail: nilanjan@hyderabad.bits-pilani.ac.in

reliability of CT dyes in practical applications. The rational correlation of molecular structure with optical response enables the predictive design of dyes with tailored absorption windows, emission color, charge-separation efficiency, and environmental responsiveness, which is essential for optimizing materials for sensing, bioimaging, nonlinear optics, and optoelectronic devices.

In this context, the present work provides a comprehensive structure–property correlation for two closely related barbituric-acid-based donor–π–acceptor chromophores by combining ground- and excited-state DFT/TD-DFT calculations with solvent-dependent PCM and conceptual DFT analyses. By systematically comparing excitation-induced geometric relaxation, Mulliken charge redistribution, electrostatic potential polarization, frontier molecular orbital topology, thermodynamic parameters, and global reactivity descriptors, we elucidate how subtle structural modifications decisively alter excited-state electronic behavior. The results clearly demonstrate that compound 1 retains a rigid, delocalized π-framework, with a predominantly locally excited character and weak solvent responsiveness, whereas compound 2 undergoes pronounced excitation-induced bond reorganization, strong donor-to-acceptor charge migration, and solvent-stabilized intramolecular charge-transfer behavior. Importantly, the extension of these structure–property insights to photovoltaic descriptors reveals that the enhanced excited-state polarization, favorable frontier orbital alignment, and efficient charge separation in compound 2 translate into superior theoretical suitability for dye-sensitized solar cell applications, while the limited charge-transfer character of compound 1 restricts its photovoltaic performance.

Results and discussion

Variation of the structural parameters at different electronic states

The optimized geometrical parameters provided a detailed comparison of the excited-state structural responses of the barbituric-acid-based chromophores, clearly differentiating the rigid electronic behavior of 1 from the excitation-induced electronic reorganization observed in 2 (Fig. 1).[9] In the case of 1, all key bonds along the barbituric acid–vinylene–aryl conjugation pathway (C_{26}–N_{35}, C_{26}–O_{32}, C_{25}–C_{15}, C_{13}–C_{11}, and C_{10}–C_2) remained essentially unchanged upon excitation from S_0 to S_1, with bond-length variations close to zero. Consistently, the associated dihedral angles (C_{27}–C_{25}–C_{15}–C_{13} and C_{15}–C_{13}–C_{11}–C_{10}) retained strict planarity in both electronic states. This invariance indicated a highly rigid and preorganized π-conjugated framework, in which photoexcitation occurred without significant geometric relaxation, reflecting strong ground-state conjugation and efficient donor–acceptor electronic coupling, resulting in low reorganization energy and a predominantly locally excited character. In contrast, 2 exhibited pronounced excitation-induced bond-length modulation along the donor–acceptor axis, indicative of substantial electronic redistribution in the excited state. A marked elongation of the N_{32}–C_{31} bond (1.37 → 1.48 Å) signified a reduction in π-bond character due to electron density withdrawal from the barbituric-acid nitrogen upon excitation. Similarly, the carbonyl-associated bonds (C_{31}–O_{30} and C_{29}–O_{28}) showed noticeable elongation (Δ = +0.04 Å), consistent with the antibonding orbital population and partial weakening of the C=O character in the S_1 state. In contrast, a slight shortening of the C_3–C_2 bond (Δ = −0.01 Å) suggested an enhanced π-delocalization and partial quinoidal stabilization along the conjugated linker.[10] Although the molecular backbone of 2 remained largely planar in the excited state, as reflected by dihedral angles close to 180° (*e.g.*, C_{29}–C_{26}–C_{24}–C_{22}: 179.99° → 179.43°), these subtle deviations indicated localized geometric relaxation that stabilized the polarized excited-state charge distribution.

Variation of the charge distribution at different electronic states

The Mulliken charge distribution analysis in the gas phase provided atom-resolved insight into the ground-state (S_0) and

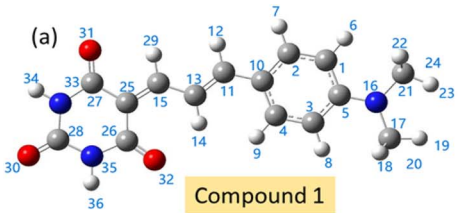

Comp 1	Ground state (S_0) (A°)	Excited state (S_1) (A°)
C26 - N35	1.40282	1.40282
C26 - O32	1.24520	1.24520
C25 - C15	1.37020	1.37020
C13 - C11	1.36536	1.36536
C10 - C2	1.41277	1.41277

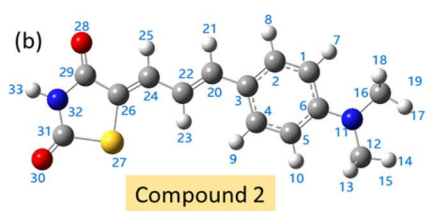

Comp 2	Ground state (S_0) (A°)	Excited state (S_1) (A°)
N32 - C31	1.37869	1.48773
C31 - O30	1.21527	1.25840
C26 - C24	1.34950	1.35520
C22 - C20	1.35951	1.35520
C29 - O28	1.23514	1.25840

Fig. 1 DFT-optimized geometries of (a) compound 1 and (b) compound 2, with atom numbering used for bond identification. The tables provide summaries of selected bond lengths (Å) in the ground state (S_0) and first singlet excited state (S_1), obtained from TD-DFT calculations.

excited-state (S_1) electronic reorganization of 1 and 2 (Fig. 2a). For 1, the S_0 charge profile showed smooth and moderate alternation along the molecular backbone, with negative charges localized on the barbituric-acid carbonyl oxygen atoms (O_{30}, O_{31}, and O_{32}) and comparatively positive charges on the imide nitrogen and terminal dialkylamino nitrogen (N_{16}), consistent with its donor–acceptor architecture. The conjugated vinylene–aryl bridge atoms (C_{10}–C_{15} and C_2–C_5) exhibited only small fluctuations around neutrality, indicating efficient π-electron delocalization and weak intrinsic ground-state polarization. Upon excitation to S_1, the charge distribution remained largely conserved, with only marginal charge amplification at the donor nitrogen (N_{16}) and slight additional negative charge accumulation on the barbituric-acid carbonyl oxygens, confirming the absence of pronounced long-range charge migration and indicating a predominantly locally excited electronic character.[11] In contrast, 2 displayed a markedly different charge evolution. In the S_0 state, negative charges were more strongly localized on the barbituric-acid carbonyl oxygen atoms and the heteroatom-substituted region, while the donor-side dialkylamino nitrogen and adjacent carbon atoms carried appreciable positive charges, establishing a clear donor–acceptor electrostatic gradient. Upon excitation to S_1, this polarization was significantly amplified: the donor nitrogen and terminal alkylated carbons became more positively charged, whereas the barbituric-acid carbonyl oxygens and neighboring acceptor-side carbons accumulated additional negative charges, providing clear evidence of net electron density transfer from the donor segment to the barbituric-acid acceptor unit.[12] The larger charge oscillations and deeper negative minima observed in the S_1 Mulliken profile of 2 correlated directly with the pronounced excitation-induced bond elongation at the N–C and C=O sites.

The electrostatic potential (ESP) surface maps further substantiated the contrasting electronic distributions and charge-transfer characteristics of 1 and 2 (Fig. 2b). For compound 1, the ESP surface displayed a relatively balanced and smoothly distributed potential across the molecular framework, with moderate negative potential (red regions) primarily localized on the barbituric-acid carbonyl oxygen atoms and mild positive potential (blue regions) around the imide N–H and peripheral alkylated amine sites. Importantly, the conjugated linker and aromatic segment exhibited largely neutral (green–yellow) potentials, indicating efficient π-electron delocalization and minimal ground-state charge separation. This ESP profile was fully consistent with the negligible $S_0 \rightarrow S_1$ bond-length variations and strict planarity observed in the optimized geometries.[13] In contrast, compound 2 exhibited a markedly polarized ESP surface, reflecting strong donor–acceptor asymmetry and enhanced intramolecular charge redistribution. Intense negative potential was concentrated on the barbituric-acid carbonyl oxygen atoms and was further amplified by the presence of the sulfur-containing substituent, which increased local polarizability and electron-withdrawing character.[14] Simultaneously, a pronounced positive potential appeared over the terminal dialkylamino donor moiety, generating a clear electrostatic gradient along the molecular long axis. The conjugated π-bridge connecting the donor and acceptor termini displayed a gradual potential transition, indicative of efficient charge migration across the molecular backbone. This pronounced ESP polarization correlated directly with the excitation-induced elongation of N–C and C=O bonds and the subtle backbone relaxation observed for 2, thereby confirming the formation of a strongly polarized intramolecular charge-transfer state.

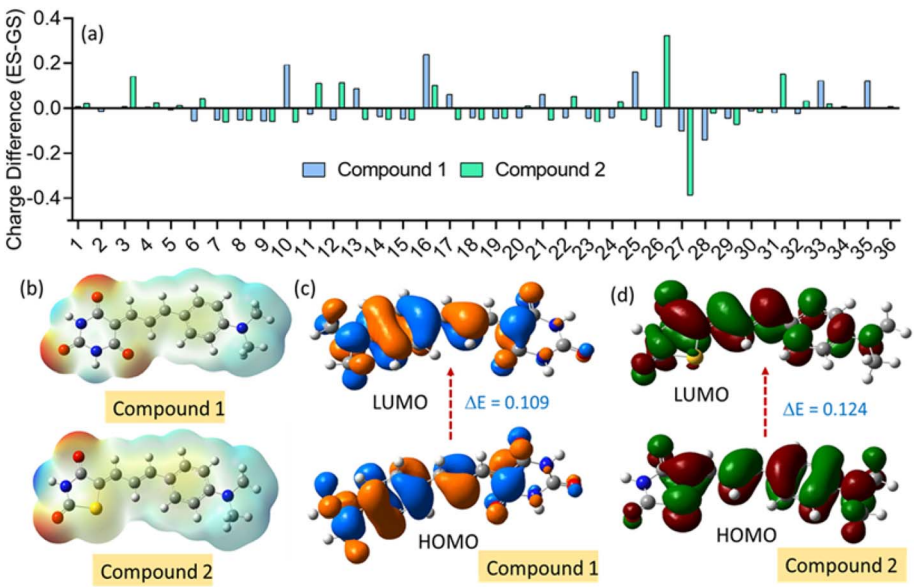

Fig. 2 (a) Atomic charge difference plots illustrating site-specific charge redistribution upon $S_0 \rightarrow S_1$ excitation for 1 and 2. (b) Electrostatic potential (ESP) surfaces of 1 and 2 mapped on the ground-state geometries. HOMO and LUMO isosurfaces of (c) compound 1 and (d) compound 2, along with the corresponding HOMO–LUMO energy gaps (hartree unit).

NBO analysis

The natural population analysis revealed significant electron density accumulation on the acceptor heteroatoms of the barbituric acid unit in both chromophores. For example, in compound 1, the carbonyl oxygen atoms exhibited charges of −0.615, −0.612, and −0.621 e, while the adjacent nitrogen atom carried a charge of −0.678 e, confirming strong electron density localization on the acceptor fragment. In contrast, the donor nitrogen in compound 1 showed a comparatively low electron density (−0.414 e), indicating relatively weak donor–acceptor polarization. For compound 2, the donor nitrogen carried a substantially high electron density (−0.677 e), which promoted strong charge delocalization along the conjugated backbone toward the barbituric-acid acceptor unit. The acceptor heteroatoms in compound 2 also displayed significant negative charges (*e.g.*, −0.583 e and −0.552 e on the carbonyl oxygen atoms and −0.682 e on the adjacent nitrogen), confirming pronounced donor–acceptor polarization. These NBO-derived charge distributions were fully consistent with the trends obtained from Mulliken population analysis, as well as with the frontier molecular orbital distributions and excitation-induced structural variations discussed in the manuscript. Therefore, the qualitative conclusions regarding the predominantly locally excited character of compound 1 and the strong intramolecular charge-transfer character of compound 2 remained unchanged when evaluated using the more robust NBO population scheme (Table S1).

Effect of solvents on the distribution of frontier molecular orbitals

The frontier molecular orbital (FMO) analysis in the ground state (in gas phase) provided direct insight into the contrasting electronic structures and charge-transfer propensities of the two barbituric-acid-based chromophores (Fig. 2c and d). For compound 1, the HOMOs were extensively delocalized over the conjugated π-framework, spanning the aromatic ring and vinylene bridge and partially extending toward the barbituric acid core, with only limited localization on the terminal substituents. The corresponding LUMO was likewise broadly distributed along the same conjugated backbone, including the barbituric acid moiety, indicating strong spatial coincidence and substantial orbital overlap between the frontier orbitals. Such pronounced HOMO–LUMO overlap suggested that the lowest-energy electronic transition in 1 was dominated by a π–π* excitation, with minimal spatial charge separation.[15] In contrast, compound 2 exhibited a distinctly different FMO topology, reflecting enhanced donor–acceptor differentiation. The HOMO orbitals were primarily localized on the electron-rich donor segment, encompassing the terminal dialkylamino group and the adjacent conjugated π-bridge, whereas the LUMOs were strongly shifted toward the electron-deficient barbituric-acid acceptor unit and the heteroatom-substituted region. This pronounced spatial separation between the HOMO and LUMO clearly indicated a donor-to-acceptor charge-transfer pathway upon excitation.[16] The reduced orbital overlap facilitated efficient electron density migration from the donor end toward the barbituric acid core, thereby rationalizing the significant excitation-induced bond elongation at the N–C and C=O sites, the enhanced ESP surface polarization, and the stabilization of a strongly polarized ICT excited state.

The solvent-dependent PCM calculations further elucidated the distinct electronic responses of 1 and 2 to their surrounding dielectric environments (Fig. 3a). For compound 1, the inclusion of solvent effects led to a pronounced increase in the molecular dipole moment from ∼10 D in the gas phase to approximately 15.3 D in polar media, such as methanol and acetonitrile, indicating the enhanced stabilization of an already polar electronic distribution. Correspondingly, the total electronic energy was significantly lowered in solution, reflecting favorable solute–solvent electrostatic interactions. Despite this stabilization, the HOMO–LUMO energy gap exhibited only marginal variation across solvents, as both HOMO and LUMO energies underwent small and nearly parallel shifts, thereby preserving the overall gap. Even in nonpolar heptane, only minor changes in the frontier orbital energies were observed. This weak solvent dependence of the HOMO–LUMO gap was consistent with the largely delocalized frontier orbitals and minimal charge separation in 1, corroborating its predominantly locally excited electronic character and the rigid π-conjugated framework.[17] In contrast, 2 displayed markedly strong solvent sensitivity, reflecting its intrinsically polarized donor–acceptor architecture. The dipole moment increased from ∼8.2 D in the gas phase to ∼12.3 D in methanol and remained elevated in acetonitrile, highlighting the significant solvent-induced stabilization of the polarized electronic structure. The total electronic energy was substantially lowered in polar solvents, consistent with the efficient dielectric stabilization of charge-separated states. Notably, the HOMO and LUMO energies responded more asymmetrically to solvent polarity than in compound 1, leading to the more pronounced modulation of the HOMO–LUMO gap across different media (Fig. 3b). Polar solvents preferentially stabilized the LUMO localized on the barbituric-acid acceptor unit while simultaneously influencing the donor-localized HOMO, thereby tuning the effective electronic gap.[18] Even in nonpolar heptane, residual stabilization was observed due to the intrinsic molecular polarity.

The PCM approach treated the solvent as a polarizable dielectric continuum, and therefore, it accounted for only nonspecific electrostatic stabilization. Specific solute–solvent interactions, particularly hydrogen bonding involving the carbonyl oxygen atoms and imide N–H groups of the barbituric acid unit, were not explicitly described. In protic solvents, such as methanol, directional hydrogen bonding to the acceptor carbonyl sites could further stabilize polarized ground and excited states, potentially enhancing charge localization and intramolecular charge-transfer character beyond the dielectric effects captured here. Accordingly, the solvent-dependent trends discussed in this work primarily reflect bulk polarity effects, and explicit solvent models would be required for a quantitative assessment of hydrogen-bond-mediated stabilization.

Effect of solvents on thermodynamic parameters

The PCM-based solvent-dependent thermodynamic analysis highlighted the contrasting stabilization mechanisms operative

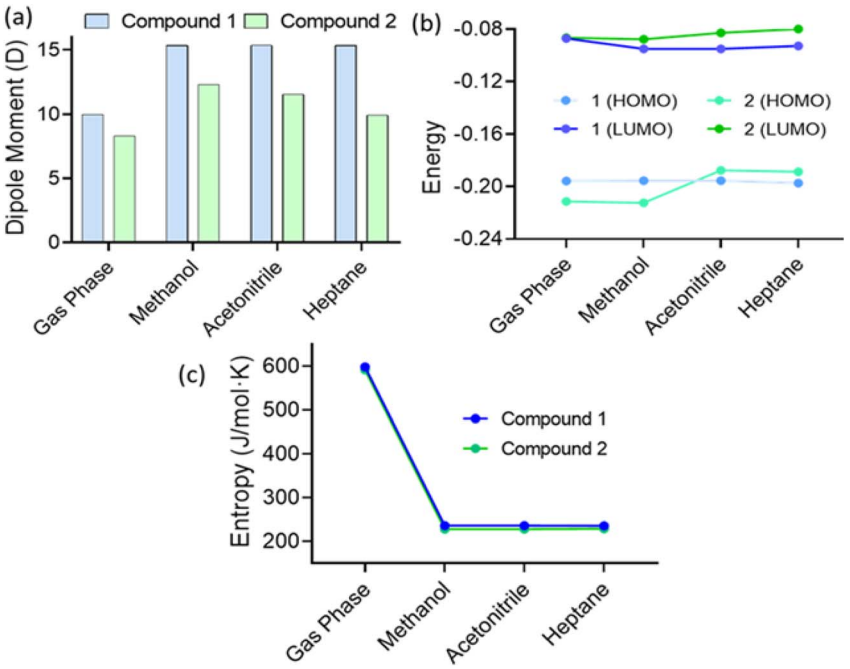

Fig. 3 (a) Variation in the dipole moments (D) of 1 and 2 from the gas phase to polar (methanol and acetonitrile) and nonpolar (heptane) solvents. (b) Solvent-induced modulation of the frontier molecular orbital energies (HOMO and LUMO) of 1 and 2. (c) Entropy changes across different media, revealing a significant reduction upon solvation for both compounds 1 and 2.

in 1 and 2. For compound 1, transfer from the gas phase to solution resulted in a substantial decrease (more negative values) in both the Gibbs free energy (G) and enthalpy (H), indicating effective thermodynamic stabilization by the solvent environment (Fig. 3c). The close similarity of the G and H values in methanol, acetonitrile, and heptane suggested that this stabilization was largely nonspecific and electrostatic in nature, arising primarily from general dielectric screening rather than from strong, directional solute–solvent interactions. Notably, the entropy (S) decreased sharply from 598.7 J mol^{-1} K^{-1} in the gas phase to approximately 236 J mol^{-1} K^{-1} in solution, reflecting restricted molecular degrees of freedom upon solvation due to cavity formation and solvent ordering around the solute. The near-identical entropy values observed across different solvents further implied that solvation imposed a comparable level of structural constraint, irrespective of solvent polarity, consistent with the rigid, weakly polarized electronic structure of 1 and its limited charge redistribution.[19] In contrast, compound 2 exhibited a more pronounced and systematic solvent response, consistent with its relatively strong donor–acceptor character. Solvation induced a greater decrease in both G and H than in compound 1, indicating the enhanced stabilization of the intrinsically polarized molecular framework. Polar solvents, such as methanol and acetonitrile, stabilized compound 2 more effectively than the gas phase, as evidenced by more negative free energies, while even nonpolar heptane provided significant stabilization due to the inherent molecular dipole. The entropy reduction was again substantial, decreasing from 592 J mol^{-1} K^{-1} in the gas phase to approximately 228 J mol^{-1} K^{-1} in solution. It is important to note that compound 2 already exhibited a slightly lower gas-phase entropy than compound 1, indicating intrinsic structural differences between the two chromophores. Therefore, the low absolute entropy values observed in solution for compound 2 could not be attributed solely to enhanced solvent organization. Rather, the overall entropy reduction upon solvation likely reflected a combined effect of inherent molecular rigidity and solvent-induced ordering around the polarized donor–acceptor framework.[20]

Effect of solvents on global reactivity parameters

The solvent-dependent conceptual DFT (CDFT) parameters provided a coherent thermodynamic-electronic description of how solvation modulated the reactivity profiles of compounds 1 and 2. The HOMO and LUMO energies of 1 remained nearly invariant across different solvents, resulting in only a small reduction in the HOMO–LUMO gap in the polar media (from 0.1087 in the gas phase to ~0.1004 in methanol and acetonitrile), followed by a slight recovery in nonpolar heptane. This marginal gap modulation was reflected in the nearly constant global hardness (η) and the corresponding increase in global softness (S) in polar solvents, indicating a modest enhancement in polarizability without altering the intrinsic electronic rigidity of the π-conjugated framework. The electronegativity (χ) and chemical potential (μ) showed minimal sensitivity to solvent polarity, confirming that solvation stabilized the frontier orbitals of 1 in a nearly symmetric manner.[21] Notably, the electron affinity (A) and electrophilicity index (ω) increased slightly in polar solvents, suggesting the weak solvent-assisted stabilization of the acceptor character; however, the charge-

transfer descriptor (ΔN) remained nearly constant, reinforcing that 1 did not undergo significant solvent-induced charge separation. Overall, these trends indicated that solvation primarily provided dielectric stabilization rather than fundamentally altering the thermodynamic reactivity profile of 1. In contrast, compound 2 exhibited a more pronounced and solvent-dependent response consistent with its donor–acceptor architecture. In polar solvents, such as methanol and acetonitrile, the HOMO–LUMO gap showed noticeable modulation relative to the gas phase, accompanied by the solvent-dependent redistribution of global hardness and softness, indicative of enhanced electronic adaptability.[22] The electronegativity (χ) and chemical potential (μ) shifted more significantly in the polar media, reflecting the relatively strong stabilization of the polarized electronic structure. Importantly, the electron donor (ω^-) and electron acceptor (ω^+) capacities displayed greater solvent sensitivity than those of 1, highlighting the asymmetric stabilization of donor- and acceptor-localized orbitals.[23] The electrophilicity index (ω) and charge-transfer parameter (ΔN) also varied more strongly with solvent polarity, signifying an increased propensity for intermolecular and intramolecular charge transfer in polar environments.[24] Although the partial relaxation of these effects was observed in nonpolar heptane, the values remained distinct from those of the gas phase due to the intrinsic dipole moment of 2, further supporting its solvent-tunable intramolecular charge-transfer character.

Table 1 Solvent-dependent conceptual DFT descriptors of compound 1 and compound 2 were calculated in the gas phase and in different solvent environments (MeOH, CH_3CN, and C_7H_{15}) using PCM

Parameter	Comp.	Gas	MeOH	CH_3CN	C_7H_{15}
E_{HOMO}	1	−0.1958	−0.1955	−0.1955	−0.1974
	2	−0.2114	−0.2125	−0.1877	−0.1887
I	1	0.1955	0.1955	0.1955	0.1974
	2	0.2114	0.2125	0.1877	0.1887
E_{LUMO}	1	−0.0871	−0.0951	−0.0951	−0.0928
	2	−0.0866	−0.0877	−0.0828	−0.0800
ΔE	1	0.1087	0.1004	0.1004	0.1046
	2	0.1248	0.1249	0.1048	0.1087
γ	1	−0.8913	−0.8996	−0.8996	−0.8954
	2	−0.8752	−0.8753	−0.8952	−0.8913
A	1	0.0871	0.0951	0.0951	0.0928
	2	0.0866	0.0877	0.0828	0.0800
ω^+	1	0.1202	0.1439	0.1440	0.1354
	2	0.1112	0.1136	0.1134	0.1057
ω^-	1	0.261	0.289	0.289	0.280
	2	0.260	0.263	0.248	0.240
χ	1	0.1415	0.1453	0.1453	0.1451
	2	0.1490	0.1502	0.1353	0.1344
η	1	0.1087	0.1004	0.1004	0.1046
	2	0.1248	0.1249	0.1048	0.1087
S	1	9.1988	9.9612	9.9641	9.5629
	2	8.0147	8.0218	9.5383	9.1996
μ	1	−0.1415	−0.1453	−0.1453	−0.1451
	2	−0.1490	−0.1502	−0.1353	−0.1344
ΔN	1	−1.3016	−1.4473	−1.4478	−1.3876
	2	−1.1942	−1.2048	−1.2901	−1.2360
ω	1	0.0921	0.1051	0.1052	0.1007
	2	0.0890	0.0905	0.0872	0.0830

Effect of solvents on polarizability

Further, the ground-state (S_0) polarizability analysis of 1 and 2 provided quantitative insight into how π-conjugation and donor–acceptor asymmetry influenced the electronic deformability of these barbituric-acid-based chromophores. The exact polarizability tensor components of 1 (547.37, 0.241, 174.71, −0.01, 0.012, and 58.58) indicated a strongly anisotropic polarizability, with the dominant contribution aligned along the extended molecular conjugation axis.[25] The negligible off-diagonal tensor elements confirmed minimal cross-coupling between orthogonal polarization directions, consistent with a rigid, planar backbone and efficient π-electron delocalization. Accordingly, the isotropic polarizability of 260.218 au (38.56 $Å^3$) reflected a relatively soft and deformable electron cloud arising from uniform charge delocalization across the donor–π–acceptor framework. In comparison, compound 2 exhibited exact polarizability tensor components of 516.87, −2.73, 178.36, −0.002, 0.005, and 60.13, also demonstrating pronounced anisotropy dominated by polarization along the molecular long axis. However, the slightly reduced principal tensor value and marginally enhanced asymmetry suggested increased electron localization near the barbituric acid–heteroatom (S-containing) region, in agreement with the ESP and Mulliken charge analyses.[26] Consequently, the isotropic polarizability of 2 was marginally lower (251.77 au, 37.30 $Å^3$) than that of 1, indicating a somewhat more rigid ground-state electron distribution despite its stronger intrinsic donor–acceptor character. Therefore, these results reinforced the view that compound 1 behaved as a rigid yet electronically soft chromophore in S_0, while compound 2 was predisposed toward strong excitation-induced polarization and solvent-tunable ICT responses (Table 1).[27]

The HOMO–LUMO energy gap (ΔE) for compound 1 was 0.109 hartree, while compound 2 exhibited a slightly larger gap of 0.124 hartree, indicating marginally stronger electronic stabilization in the latter.

While compound 1 displayed a relatively large absolute dipole moment and strong solvent-induced polarity increase, the frontier orbital distribution in compound 2 indicated significant spatial separation between donor and acceptor regions. Consequently, compound 2 was expected to exhibit more pronounced intramolecular charge transfer upon excitation despite its low ground-state dipole moment.

Predicted photovoltaic performance and DSSC suitability

The photovoltaic behaviors of 1 and 2 were quantitatively predicted using electron-injection driving force, excited-state dipole moment, charge-separation capability, light-harvesting efficiency, and reorganization energy, which collectively determined their suitability as dye sensitizers for DSSC applications.[28] The electron-injection driving force of 1 relative to the TiO_2 conduction band ($E_{CB} = -4.0$ eV) was $\Delta G_{inject} = -0.02$ eV, indicating thermodynamically unfavourable electron injection into TiO_2. This limitation was compounded by a moderate excited-state dipole moment ($\mu^* = 15.3$ D; $\Delta\mu = 5.3$ D from $\mu =$

10.0 D), reflecting insufficient long-range charge separation to suppress interfacial recombination. Its light-harvesting efficiency (LHE = 0.78), derived from an oscillator strength of $f = 0.65$, suggested only moderate photon absorption, while the low reorganization energy ($\lambda = 0.10$ eV), arising from its rigid and planar π-framework, although favorable for fast electronic relaxation, could not compensate for the weak injection thermodynamics and limited excited-state polarization. Consequently, compound 1 did not meet the key electronic criteria required for an efficient DSSC sensitizer and was better suited as a structurally robust reference or auxiliary light-harvesting component rather than a primary dye. In contrast, compound 2 exhibited a strongly favorable DSSC profile, with a positive electron-injection driving force of $\Delta G_{inject} = +0.38$ eV, ensuring thermodynamically viable electron transfer from the excited dye into the TiO_2 conduction band. This was reinforced by a large excited-state dipole moment ($\mu^* = 19.8$ D) and substantial dipole change ($\Delta\mu = 11.6$ D from $\mu = 8.2$ D), confirming efficient intramolecular charge separation critical for minimizing recombination losses. The high light-harvesting efficiency of 2 (LHE = 0.91), derived from its strong oscillator strength ($f = 1.05$), indicated superior visible-light absorption, while its moderate reorganization energy ($\lambda \approx 0.24$ eV) remained within the optimal range for charge-transfer dyes in DSSCs. Taken together, the quantitative descriptors unambiguously identified compound 2 as a promising DSSC sensitizer, whereas compound 1 was limited by insufficient electron-injection capability and weak excited-state charge separation, resulting in only moderate photovoltaic applicability.

Conclusion

In summary, this work established a comprehensive and internally consistent structure–property-function relationship for two closely related barbituric-acid-based donor–π–acceptor chromophores through a synergistic combination of ground- and excited-state DFT/TD-DFT calculations, solvent-dependent PCM analysis, and conceptual DFT descriptors. Despite their close structural similarity, the two chromophores exhibited fundamentally distinct excited-state behaviors, governed by subtle differences in donor–acceptor asymmetry and heteroatom substitution. Compound 1 retained an exceptionally rigid and planar π-conjugated framework upon photoexcitation, displaying negligible bond-length redistribution, strong HOMO–LUMO spatial overlap, weak solvent dependence, minimal Mulliken charge migration, and uniform electrostatic potential distribution. These features collectively identified its lowest excited state as predominantly locally excited in nature, resulting in limited excited-state polarization and modest electronic adaptability. In contrast, compound 2 exhibited pronounced excitation-induced geometric relaxation along the donor–acceptor axis, accompanied by significant bond-order modulation, amplified Mulliken charge redistribution, strongly polarized electrostatic potential surfaces, and clear spatial separation of frontier molecular orbitals. Solvent-dependent PCM and conceptual DFT analyses further revealed that this polarized electronic structure was efficiently stabilized in polar environments, leading to enhanced excited-state dipole moments, tunable HOMO–LUMO gaps, and high electronic softness. These characteristics unambiguously confirmed the formation of a strongly polarized intramolecular charge-transfer excited state in compound 2. Importantly, the extension of these electronic insights to photovoltaic descriptors established a clear divergence in DSSC suitability. Compound 1 showed a marginal and thermodynamically unfavourable electron-injection driving force into the TiO_2 conduction band, moderate light-harvesting efficiency, and insufficient excited-state charge separation, restricting its applicability as an effective DSSC sensitizer. In contrast, compound 2 satisfied all key electronic criteria for DSSC operation, including a favorable positive electron-injection driving force, large excited-state dipole enhancement, high oscillator strength and light-harvesting efficiency, and an optimal reorganization energy that supports efficient interfacial charge transfer while minimizing recombination losses.

Conflicts of interest

There are no conflicts to declare.

Data availability

The data will be available from authors on reasonable request.

Supplementary information (SI) is available. See DOI: https://doi.org/10.1039/d6ra00689b.

Acknowledgements

N. D. thanks DST for the SYST grant [grant no. (SP/YO/2021/1632)] and the Ministry of Education (MOE), India, for the STARS grant (STARS2/2023-0300). N. D. thank BITS Pilani, Hyderabad campus, for financial and technical support. The authors also thank the central analytical facilities at BITS Pilani, Hyderabad, for instrumental facilities.

References

1 M. A. Rahma, B. A. Saleh, M. Y. Shubar, H. L. Saadon and A. Marhoon, Synthesis, characterization, nonlinear optical properties, and DFT analysis of a new azo-Schiff base dye, *J. Mol. Struct.*, 2026, **1355**, 145051.

2 P. K. Dhanya, J. Arjun, N. Kaur and R. R. Pillai, Solvent-dependent electronic, photophysical and nonlinear optical properties of azulene-based push–pull chromophores: A DFT approach, *J. Mol. Graph. Model.*, 2026, **142**, 109180.

3 S. Schinca Vanini and G. F. Cabeza, Decoding the optical band gap: A methodological comparison using DFT-based absorption spectra, *Next Mater.*, 2026, **10**, 101498.

4 L. Li, C. Huo, P. Liu, F. Yang, L. Guo, Z. Wang and X. Xuan, Comparative study of three new benzoindole-based fluorescent building blocks: Synthesis, crystal structure, optical properties, and DFT calculations, *J. Mol. Struct.*, 2025, **1348**, 143575.

5 P. O. Gupta, Z. Khan, Z. A. Siddiqui, S. J. Sharma, S. More and N. Sekar, Carbazole-based donor with different π-spacers for nonlinear optical properties: Synthesis, photophysical properties, viscosity, acidochromism, and DFT studies, *J. Mol. Struct.*, 2025, **1336**, 142006.

6 H. F. Ali, M. Adeel, U. Aiman, S. Jamal, M. Haroon and T. S. Ahamad, spectral characterization and nonlinear optical exploration of potent fluorene-based compounds: A DFT-refined experimental study, *J. Mol. Struct.*, 2026, **1349**, 143630.

7 B. Abdelaziz, S. Bouazizi, B. Gassoumi, S. Patanè and S. Ayachi, DFT and molecular dynamics study of the optical and electronic properties of nitrobenzofurazan-based molecules for photovoltaic and nonlinear optical applications, *Mater. Chem. Phys.*, 2025, **332**, 130269.

8 V. H. Rezvan, S. B. Pour and J. J. Sardroodi, Molecular structures and optical properties of Schiff bases derived from pyrrole alkyl ketones and 1-aminophthalazine: DFT calculations, *Results Chem.*, 2024, **12**, 101907.

9 S. K. Mohamed, S. A. Siddique, S. H. H. Younes, S. E. M. Elgarhy, R. Al-Salahi, H. A. Abuelizz, J. T. Mague, E. M. M. Abdel-Raheem and Y. El Bakri, Synthesis, crystallographic analysis, and nonlinear optical properties of a novel thiosemicarbazone derivative: A DFT study, *J. Mol. Struct.*, 2025, **1348**, 143597.

10 S. Podder, S. Dey and A. Chatterjee, Exploration of DFT-based static and dynamic nonlinear optical activity of an acridine-1,8-dione derivative, *J. Indian Chem. Soc.*, 2025, **102**, 102100.

11 H. A. Khan, M. Irfan, S. G. Khan, S. Bibi, A. Ali, I. Shafiq, N. Alhokbany, M. Haroon and H. Y. Gondal, Facile synthesis, spectroscopic, electronic and nonlinear optical properties of 1,2,4-triazole-based derivatives: An experimental and DFT approach, *J. Mol. Struct.*, 2025, **1322**, 140576.

12 S. Paul and N. Dey, Solvent-Assisted Prototopic Switching of Norharmane Along Hydrogen-Bonded Network: Assessing the Precise Length of Network, *J. Phys. Org. Chem.*, 2025, **38**, e4678.

13 E. B. Ariza Paez, S. Curcio, N. P. Neme, M. J. S. Matos, R. S. Correa, F. J. Pereira, F. F. Hilário, T. Cazati and J. G. Taylor, Synthesis, photophysical and electrochemical properties of novel and highly fluorescent difluoroboron flavanone β-diketonate complexes, *New J. Chem.*, 2020, **44**, 14615–14631.

14 Y. Zhou, S. Maisonneuve, L. Casimiro, P. Retailleau, J. Xie, F. Maurel and R. Métivier, Photoisomerization of a 4-dicyanomethylene-2-methyl-6-(p-dimethylaminostyryl)-4H-pyran analog dye: A combined photophysical and theoretical investigation, *Phys. Chem. Chem. Phys.*, 2022, **24**, 6282–6289.

15 P. Kimber, P. Goddard, I. A. Wright and F. Plasser, The role of excited-state character, structural relaxation, and symmetry breaking in enabling delayed fluorescence activity in push–pull chromophores, *Phys. Chem. Chem. Phys.*, 2021, **23**, 26135–26150.

16 D. I. Tasgin and P. S. Sirin, Effect of structural modifications on molecular, electronic, and optical properties of phosphonate-substituted BODIPY dyes: A theoretical investigation, *ChemistrySelect*, 2021, **6**, 4677–4683.

17 S. Paul, A. Ray Choudhury and N. Dey, Dual Mode Multiple Ions Sensing *via* Analyte-Specific Modulation of Keto-Enol Tautomerization of an ESIPT Active Pyrene Derivative: Experimental Findings and Computational Rationalization, *ACS Omega*, 2023, **8**, 6349–6360.

18 B. Abdelaziz, I. Chérif, B. Gassoumi, S. Patanè and S. Ayachi, Linear and nonlinear optical responses of nitrobenzofurazan–sulfide derivatives: DFT-QTAIM investigation on twisted intramolecular charge transfer, *J. Phys. Chem. A*, 2023, **127**, 9895–9910.

19 N. M. Mahani and F. S. Mostaghni, DFT and TD-DFT study of the nonlinear optical and electronic properties of new quinoxaline acceptors for dye-sensitized solar cells, *Opt. Quant. Electron.*, 2025, **57**, 653.

20 S. Paul, R. S. Fernandes and N. P.-L. Dey, Dual Channel Sensing of Cyanide and Bisulfate Ions in Aqueous Medium: Computational Rationalization of Ion-Dependent ICT Mechanism, *New J. Chem.*, 2022, **46**, 18973–18983.

21 I. Shafiq, I. Irshad, R. Zahid, *et al.*, Exploration of promising key electronic and nonlinear optical properties of bifluorenylidene-based chromophores: A TD-DFT/DFT approach, *Sci. Rep.*, 2025, **15**, 10701.

22 P. K. Kushwaha and S. K. Srivastava, Tuning optoelectronic properties of indandione-based D–A materials by malononitrile group acceptors: A DFT and TD-DFT approach, *J. Mol. Model.*, 2024, **30**, 356.

23 E. Sarıkaya, Y. Ekincioğlu, S. Bahçeli, *et al.*, Analysis of the nonlinear optical properties, vibrational spectra, DFT method and photovoltaic performance of cyanidin-3-rutinoside chloride, *Opt. Quant. Electron.*, 2024, **56**, 1383.

24 S. Mondal, S. Paul and N. Dey, Host–guest-mediated modulation of pyrimidine charge-transfer probes by cyclodextrin nanosponges for aqueous-phase cyanide detection, *Langmuir*, 2025, **41**, 26789–26797.

25 S. Paul and N. Dey, Solvent-assisted prototropic switching of norharmane along hydrogen-bonded networks: Assessing the precise length of the network, *J. Phys. Org. Chem.*, 2025, **38**, e4678.

26 R. S. Fernandes, S. Paul, M. Klikar, F. Bureš and N. Dey, Towards portable kits for on-site colorimetric detection of aqueous hydrazine using a piperidine–thiophene–barbituric acid push–pull probe, *ChemPlusChem*, 2025, **90**, e202400492.

27 S. Paul, R. S. Fernandes and N. Dey, ppb-level, dual-channel sensing of cyanide and bisulfate ions in aqueous medium: Computational rationalization of ion-dependent ICT mechanism, *New J. Chem.*, 2022, **46**, 18973–18983.

28 O. M. I. Adly, A. Taha, S. A. Fahmy and M. A. Ibrahim, TD-DFT calculations, dipole moments, and solvatochromic properties of 2-aminochromone 3-carboxaldehyde and its hydrazone derivatives, *RSC Adv.*, 2023, **13**, 26587–26603.